



DEVELOPMENT OF A TOMOGRAPHIC ATMOSPHERIC MONITORING SYSTEM BASED ON DIFFERENTIAL OPTICAL ABSORPTION SPECTROSCOPY

RUI FILIPE CANTARINO VALENTE DE ALMEIDA

Master in Biomedical Engineering

BIOMEDICAL ENGINEERING

NOVA University Lisbon
September, 2022



NOVA

NOVA SCHOOL OF
SCIENCE & TECHNOLOGY

DEPARTMENT
OF PHYSICS

DEVELOPMENT OF A TOMOGRAPHIC ATMOSPHERIC MONITORING SYSTEM BASED ON DIFFERENTIAL OPTICAL ABSORPTION SPECTROSCOPY

RUI FILIPE CANTARINO VALENTE DE ALMEIDA

Master in Biomedical Engineering

Adviser: Prof. Dr. Pedro Vieira
Auxilliary Professor, NOVA University Lisbon

BIOMEDICAL ENGINEERING

NOVA University Lisbon
September, 2022

Development of a Tomographic Atmospheric Monitoring System based on Differential Optical Absorption Spectroscopy

Copyright © Rui Filipe Cantarino Valente de Almeida, NOVA School of Science and Technology, NOVA University Lisbon.

The NOVA School of Science and Technology and the NOVA University Lisbon have the right, perpetual and without geographical boundaries, to file and publish this dissertation through printed copies reproduced on paper or on digital form, or by any other means known or that may be invented, and to disseminate through scientific repositories and admit its copying and distribution for non-commercial, educational or research purposes, as long as credit is given to the author and editor.

To my parents.

ACKNOWLEDGEMENTS

First and foremost, I need to thank FCT NOVA and FutureCompta, for having me and letting me work with them and develop this thesis. In addition, I want to acknowledge the contribution from the Portuguese Foundation for Science and Technology, who funded this work through the NOVA I4H doctoral programme, grant PDE/B-DE/114549/2016.

I would also like to thank my advisor, Prof. Pedro Vieira, for all the support he has given me, on many levels and throughout the years.

To my friends, old and new, I extend my utmost gratitude for helping me tilt my head back and laugh once in a while.

Finally, to my family, without whom I would have never been able to do anything, much less something as significant as what I present in this dissertation.

“I know the pieces fit, 'cause I watched them fall away. ”
(TOOL - Schism)

“Silenzio, Bruno! ” (Luca Paguro)

ABSTRACT

The aim of this thesis is to describe the design and development of a proof of concept for a commercially viable large area atmospheric analysis tool, for use in trace gas concentration mapping and quantification.

Atmospheric monitoring is a very well researched field, with dozens of available analytical systems and subsystems. However, current systems require a very important compromise between spatial and operational complexity. We address this issue asking how we could integrate the [Differential Optical Absorption Spectroscopy \(DOAS\)](#) atmospheric analysis technique in a [Unmanned Aerial Vehicle \(UAV\)](#) with tomographic capabilities.

Using a two-part methodology, I proposed two hypothesis for proving the possibility of a miniaturised tomographic system, both related to how the spectroscopic data is acquired. The first hypothesis addresses the projection forming aspect of the acquisition, its matrix assembly and the resolution of the consequent equations. This hypothesis was confirmed theoretically by the development of a simulation platform for the reconstruction of a trace gas concentration mapping.

The second hypothesis deals with the way in which data is collected in spectroscopic terms. I proposed that with currently available equipment, it should be possible to leverage a consequence of the Beer-Lambert law to produce molecular density fields for trace gases using passive [DOAS](#). This hypothesis was partially confirmed, with definite conclusions being possible only through the use of complex autonomous systems for improved accuracy.

This work has been a very important first step in the establishment of [DOAS](#) tomography as a commercially viable solution for atmospheric monitoring, although further studies are required for definite results. Moreover, this thesis has conducted to the development of a [DOAS](#) software library for Python that is currently being used in a production environment. Finally, it is important to mention that two journal articles were published from pursuing this work, both in important journals with Impact Factors over 3.0.

Keywords: [DOAS](#), tomography, [UAV](#), drones

RESUMO

Era o objectivo deste trabalho descrever o processo de desenho e implementação de uma prova de conceito para um sistema de avaliação atmosférica comercialmente viável, para uso no mapeamento das concentrações de compostos traço na atmosfera.

A avaliação atmosférica é um campo muito estudado, estando no presente momento disponíveis para instalação diversos sistemas e subsistemas com estas capacidades. No entanto, é marcante o compromisso que se verifica entre a resolução espacial e a complexidade operacional destes equipamentos. Nesta tese, desafio este problema e levanto a questão sobre como se poderia desenvolver um sistema com os mesmos fins, mas sem este premente compromisso.

Usando uma metodologia a duas partes, proponho duas hipóteses para comprovar a exequibilidade deste sistema. A primeira diz respeito à formação da matriz tomográfica e à resolução das equações que dela derivam e que formam a imagem que se pretende. Confirmei esta hipótese teoricamente através do desenvolvimento de uma plataforma de simulação para a reconstrução tomográfica de um campo de concentrações fantoma.

A segunda é dirigida a aquisição de dados espectroscópicos. Proponho que com o material presentemente disponível comercialmente, deverá ser possível aproveitar uma consequência da lei de Beer-Lambert para retirar os valores de concentração molecular de gases traço na atmosfera. Foi apenas possível validar esta hipótese parcialmente, sendo que resultados mais conclusivos necessitariam de equipamentos automatizados dos quais não foi possível dispôr.

No final, este trabalho constitui um importante primeiro passo no estabelecimento da técnica de [DOAS](#) tomográfico como uma alternativa comercialmente viável para a análise atmosférica. Ademais, o desenvolvimento desta tese levou à escrita de uma biblioteca em Python para análise de dados [DOAS](#) actualmente usada em ambiente de produção. Por fim, importa realçar que dos trabalhos realizados no decorrer da tese foram publicados dois artigos em revistas científicas com *Impact Factor* acima de 3.

Palavras-chave: [DOAS](#), tomografia, drones

CONTENTS

List of Figures	x
List of Tables	xi
List of Listings	xii
Acronyms	xiii
1 Theoretical Background	1
1.1 Unmanned Aerial Vehicle	1
1.2 Optical Systems	2
1.2.1 Telescopes	3
1.2.2 Spectrometers	4
1.3 DOAS	5
1.3.1 Types of DOAS experiments	8
1.4 Important Notes on DOAS in practice	13
1.4.1 Cross section conditioning	13
1.4.2 Spectral Calibration	14
1.5 Tomographic algorithms and reconstruction techniques	16
1.5.1 Iterative Tomographic Reconstruction Methods	21
1.5.2 Discretisation - The Siddon Algorithm	23
Bibliography	27
Annexes	

LIST OF FIGURES

1.1	General schematic for an optical system, as relevant to the work of this thesis. Its function is to gather environment light and format it as data.	3
1.2	The most basic form of telescope. The second lens (eyepiece) magnifies the image produced by the first lens (the objective) [16]	3
1.3	Basic schematics for the two types of telescopes presented.	4
1.4	Basic schematics for the two types of telescopes presented.	5
1.5	Simplified schematic flowchart of the DOAS algorithm, including the non-linear part.	9
1.6	Active DOAS schematic.	9
1.7	Passive DOAS schematic.	10
1.8	Several examples of possible passive DOAS experiment geometries. All these examples use only the light from an astronomical source to detect many atmospheric trace gases. All these examples were taken from [23].	11
1.9	Occultation measurement schematic representation [23]	11
1.10	Schematic representation of the limb satellite measurement geometry.	12
1.11	Schematic representation of the nadir satellite measurement geometry.	12
1.12	Before being used in DOAS calculations, literature trace gas cross section spectra must undergo a conditioning process to make sure they are compatible with the current experiment's instruments. Figure adapted from [4]	14
1.13	This figure, taken from [4], shows the difference between NO ₂ cross sections. The red line comes from the literature, and has been conditioned to the experiment spectrometer. The blue line was actually collected with that device. The slight discrepancies that can be observed are calibration defects.	15
1.14	High resolution solar spectrum commonly used to calibrate the various spectral signals in DOAS experiments [10].	16
1.15	Schematic representation for coordinate setting. The image depicts a parallel projection setting [21].	18
1.16	The Fourier Slice Theorem (FST), a schematic representation [2].	19
1.17	Schematic representation of an equiangular fan-beam projection, taken from [20].	21
1.18	Grid and pixel definition, as they appear in the original article by Robert Siddon [28]. Pixels are "formed"by intersecting the ray (here going from point 1 to point 2) with the superimposed grid.	23

LIST OF TABLES

LIST OF LISTINGS

ACRONYMS

CO	Carbon Monoxide 11
CO₂	Carbon Dioxide 11
CT	Computed Tomography 16
DOAS	Differential Optical Absorption Spectroscopy vii , viii , ix , x , 1 , 5 , 7 , 8 , 9 , 10 , 11 , 13 , 14 , 15 , 16 , 17
FBP	Filtered BackProjection 18 , 19 , 20 , 21
FST	Fourier Slice Theorem x , 17 , 18 , 19
FT	Fourier Transform 18 , 19
FWHM	Full Width at Half Maximum 13
H₂O	Water 11
IFT	Inverse Fourier Transform 19 , 20
MAX-DOAS	MultiAxis-DOAS 11
ROI	Region Of Interest 23 , 24 , 26
UAV	Unmanned Aerial Vehicle vii , ix , 1
WFM-DOAS	Weighting Function Modified Differential Optical Absorption Spectroscopy 11 , 12

TODO LIST

Figure:	4
Figure:	4
the image with angle notes	4
Figure:	5

THEORETICAL BACKGROUND

In the development of this thesis, I had to become familiar with several subjects, both in terms of required instrumentation and theoretical concepts.

For designing a drone based system, I had to deal with the various components that make up the vehicle itself. Designing the optical system required me to understand telescopes and spectrometers (at least from the user's point of view). Performing a tomographic inversion demanded a basic comprehension of the mathematical process behind it and how to reproduce it computationally. Finally, the spectroscopic aspect of this thesis needed quite a firm grasp on the [DOAS](#) technique.

This section aims to describe these topics, up to the level I needed to reach to complete the work.

1.1 Unmanned Aerial Vehicle

Lorem ipsum dolor sit amet, consectetur adipiscing elit. Ut purus elit, vestibulum ut, placerat ac, adipiscing vitae, felis. Curabitur dictum gravida mauris. Nam arcu libero, nonummy eget, consectetur id, vulputate a, magna. Donec vehicula augue eu neque. Pellentesque habitant morbi tristique senectus et netus et malesuada fames ac turpis egestas. Mauris ut leo. Cras viverra metus rhoncus sem. Nulla et lectus vestibulum urna fringilla ultrices. Phasellus eu tellus sit amet tortor gravida placerat. Integer sapien est, iaculis in, pretium quis, viverra ac, nunc. Praesent eget sem vel leo ultrices bibendum. Aenean faucibus. Morbi dolor nulla, malesuada eu, pulvinar at, mollis ac, nulla. Curabitur auctor semper nulla. Donec varius orci eget risus. Duis nibh mi, congue eu, accumsan eleifend, sagittis quis, diam. Duis eget orci sit amet orci dignissim rutrum.

Nam dui ligula, fringilla a, euismod sodales, sollicitudin vel, wisi. Morbi auctor lorem non justo. Nam lacus libero, pretium at, lobortis vitae, ultricies et, tellus. Donec aliquet, tortor sed accumsan bibendum, erat ligula aliquet magna, vitae ornare odio metus a mi. Morbi ac orci et nisl hendrerit mollis. Suspendisse ut massa. Cras nec ante. Pellentesque a nulla. Cum sociis natoque penatibus et magnis dis parturient montes, nascetur ridiculus mus. Aliquam tincidunt urna. Nulla ullamcorper vestibulum turpis. Pellentesque cursus luctus mauris.

Nulla malesuada porttitor diam. Donec felis erat, congue non, volutpat at, tincidunt tristique, libero. Vivamus viverra fermentum felis. Donec nonummy pellenesque ante. Phasellus adipiscing semper elit. Proin fermentum massa ac quam. Sed diam turpis, molestie vitae, placerat a, molestie nec, leo. Maecenas lacinia. Nam ipsum ligula, eleifend at, accumsan nec, suscipit a, ipsum. Morbi blandit ligula feugiat magna. Nunc eleifend consequat lorem. Sed lacinia nulla vitae enim. Pellentesque tincidunt purus vel magna. Integer non enim. Praesent euismod nunc eu purus. Donec bibendum quam in tellus. Nullam cursus pulvinar lectus. Donec et mi. Nam vulputate metus eu enim. Vestibulum pellenesque felis eu massa.

Quisque ullamcorper placerat ipsum. Cras nibh. Morbi vel justo vitae lacus tincidunt ultrices. Lorem ipsum dolor sit amet, consectetur adipiscing elit. In hac habitasse platea dictumst. Integer tempus convallis augue. Etiam facilisis. Nunc elementum fermentum wisi. Aenean placerat. Ut imperdiet, enim sed gravida sollicitudin, felis odio placerat quam, ac pulvinar elit purus eget enim. Nunc vitae tortor. Proin tempus nibh sit amet nisl. Vivamus quis tortor vitae risus porta vehicula.

Fusce mauris. Vestibulum luctus nibh at lectus. Sed bibendum, nulla a faucibus semper, leo velit ultricies tellus, ac venenatis arcu wisi vel nisl. Vestibulum diam. Aliquam pellenesque, augue quis sagittis posuere, turpis lacus congue quam, in hendrerit risus eros eget felis. Maecenas eget erat in sapien mattis porttitor. Vestibulum porttitor. Nulla facilisi. Sed a turpis eu lacus commodo facilisis. Morbi fringilla, wisi in dignissim interdum, justo lectus sagittis dui, et vehicula libero dui cursus dui. Mauris tempor ligula sed lacus. Duis cursus enim ut augue. Cras ac magna. Cras nulla. Nulla egestas. Curabitur a leo. Quisque egestas wisi eget nunc. Nam feugiat lacus vel est. Curabitur consectetur.

Suspendisse vel felis. Ut lorem lorem, interdum eu, tincidunt sit amet, laoreet vitae, arcu. Aenean faucibus pede eu ante. Praesent enim elit, rutrum at, molestie non, nonummy vel, nisl. Ut lectus eros, malesuada sit amet, fermentum eu, sodales cursus, magna. Donec eu purus. Quisque vehicula, urna sed ultricies auctor, pede lorem egestas dui, et convallis elit erat sed nulla. Donec luctus. Curabitur et nunc. Aliquam dolor odio, commodo pretium, ultricies non, pharetra in, velit. Integer arcu est, nonummy in, fermentum faucibus, egestas vel, odio.

Sed commodo posuere pede. Mauris ut est. Ut quis purus. Sed ac odio. Sed vehicula hendrerit sem. Duis non odio. Morbi ut dui. Sed accumsan risus eget odio. In hac habitasse platea dictumst. Pellentesque non elit. Fusce sed justo eu urna porta tincidunt. Mauris felis odio, sollicitudin sed, volutpat a, ornare ac, erat. Morbi quis dolor. Donec pellenesque, erat ac sagittis semper, nunc dui lobortis purus, quis congue purus metus ultricies tellus. Proin et quam. Class aptent taciti sociosqu ad litora torquent per conubia nostra, per inceptos hymenaeos. Praesent sapien turpis, fermentum vel, eleifend faucibus, vehicula eu, lacus.³

1.2 Optical Systems

Optical systems are, as far as this thesis is concerned, light capturing and digitising systems. Their purpose is to gather light from the environment at certain conditions and format it into data that one can analyse computationally and a general schematic

representation is presented in Figure 1.1. In this section, I will present the basic theoretical concepts on which I stood to design the optical system, as it is presented in the following chapters.

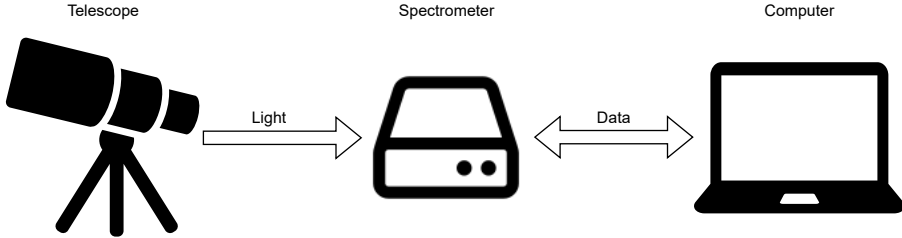


Figure 1.1: General schematic for an optical system, as relevant to the work of this thesis. Its function is to gather environment light and format it as data.

1.2.1 Telescopes

The most basic form of telescope comes from the juxtaposition of two lenses [16], as depicted in Figure 1.2. The focal point of the objective is coincident with the focal point of the eyepiece. Notice, also from the figure, that the rays reaching in the eye are parallel, so the observer can use the telescope with a relaxed eye [16].

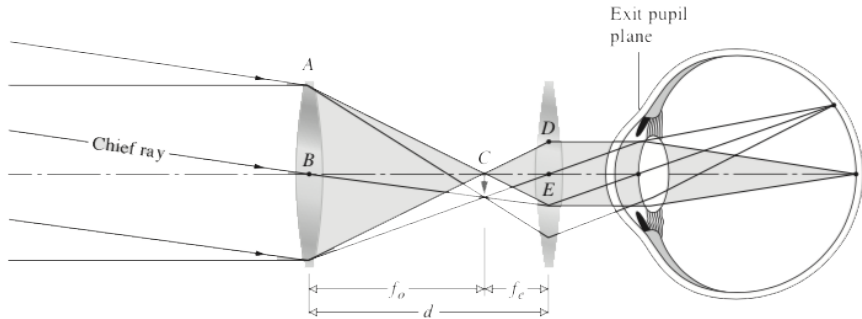
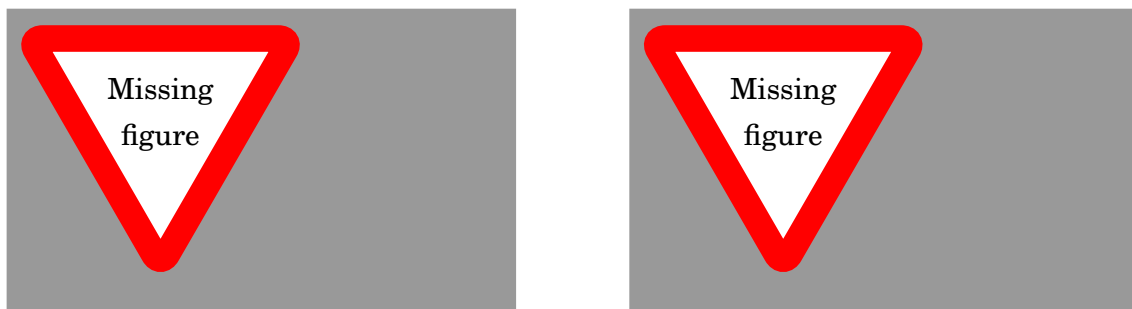


Figure 1.2: The most basic form of telescope. The second lens (eyepiece) magnifies the image produced by the first lens (the objective) [16]

It is a simple conceptual operating principle. The idea is to have a device that directionally captures ambient light and direct it into an observer's eye (or optical sensor). The amount of captured light that is captured depends on the section of the first lens, the objective (think of a constant stream of photons entering a bucket-like device). Telescopes come in various sizes and shapes. As so many devices, telescopes vary with the application the designer had in mind. Astronomical telescopes produce inverted images. This would be highly confusing for terrestrial observations (therefore, terrestrial telescopes have an erector lens). There are two main types of telescope, refractors (see Figure 1.3a) and reflectors (see Figure 1.3b). While conceptually much simpler, refraction based telescopes do have several drawbacks. They are exclusively dependent on lenses, which are difficult to manufacture. Their magnification also only depends on the length of the telescope's tube, which makes them unwieldy very quickly as large magnification implies long tubes. These inconveniences are in part solved by reflecting telescopes. They are less vulnerable to fabrication defects, since



(a) Basic schematic for a refractor telescope.

(b) Basic schematic for a reflector telescope.

Figure 1.3: Basic schematics for the two types of telescopes presented.

mirrors are much easier to produce than lenses. This brings the added benefit of having wider objectives and thus much more light entering the tube. Of at least the same importance, the focal length's dependence of the length of the tube dissipates, since the light path between the objective and the observer's eye depends now on the mirror configuration inside the telescope. For all these advantages, there are nowadays no great telescopes of refracting geometry [29, 16].

1.2.2 Spectrometers

Spectrometers are devices that measure and relate the intensity and colour of a given radiation source. In other words, it is sensitive to both the quantity and the energy of this radiation source's photons. There are many types of spectrometers. They differ on the energy range of the radiation they can measure, on the physical principle they are based on, on their applications and on the geometry of their internal components. In this thesis, the only type of spectrometer that was used a UV-Vis Czerny-Turner spectrometer. A schematic representation of this type of spectrometer is presented in Figure 1.4a, and a more realistic representation is displayed in Figure 1.4b [3]. As can be seen in both schematics, light enters the assembly through the slit and is collimated on a spherical mirror, which reflects it towards an oriented diffraction grating. The resulting diffracted light is then focused on a second spherical mirror onto a 1D linear detector array. This particularly optical assembly is highly customisable. One can choose between a variety of sensors, diffraction gratings and entrance slits, according to the spectral parameters required for one's experiment or application. Here are the most important of them.

Optical Resolution The optimal resolution comes from a correct balance between slit size and diffraction grating. Normally, for a high resolution application one would opt by using a high number of lines for the diffraction grating and a very small slit. Choose an excessive number of lines and the wavelength becomes too limited; choose an excessively small slit and there will not be enough light going through the system;

Sensitivity photometric sensitivity (how much light do we need to get a signal) and chemometric sensitivity (the smallest absorbance difference that can be measured by the device) are important device features that need to be considered

the image
with angle
notes

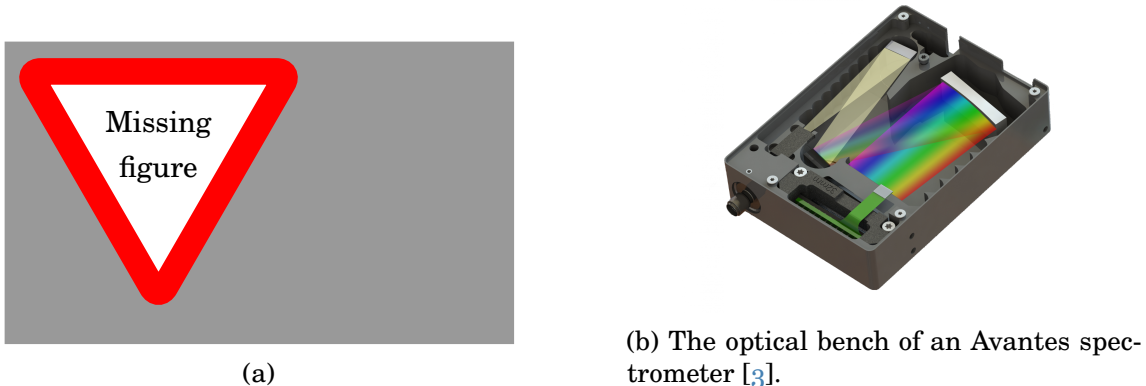


Figure 1.4: Basic schematics for the two types of telescopes presented.

a-priori:

Sensor / Detector the type of measurement being made determines the types of sensors that can be used. For instance, faster detectors are normally good choices in abundant light conditions that allow for lower integration times.

Finally, the choice of spectrometer should also include into consideration some less desirable, but inescapable, features of these devices. The most important of these is the thermal stability. Temperature variation produces slight changes in the spectrometer's optical bench and surrounding structures, which means that each part of the detector is exposed to a slightly different section of the spectrum, which naturally leads to different signal results. Commercial spectrometer manufacturers normally provide quality control measurements for the device's thermal stability values [22, 3].

1.3 DOAS

Differential Optical Absorption Spectroscopy is a well established absorption spectroscopy technique that is widely used in the field of atmospheric studies [23]. In this section, I present a short introduction to the field. The first part of this introduction is based on [31], an article we have published in 2017, marking the conclusion of the initial studies for this PhD thesis. The second and last part refers to additional research that I have conducted since then.

DOAS itself is based on Lambert–Beer’s law, which can be written as [23]

$$I(\lambda) = I_0(\lambda) \cdot \exp(-\sigma(\lambda) \cdot c \cdot L), \quad (1.1)$$

Where λ is the wavelength of the emitted light; $I(\lambda)$ is the light intensity as measured by the system; $I_0(\lambda)$ is the intensity of the light as emitted by the source; and $\sigma(\lambda)$ is the absorption cross section of absorber, which is wavelength dependent; c is the concentration of the absorber we want to measure.

This law allows the definition of optical thickness (τ) [23]:

$$\tau(\lambda) = \ln \left(\frac{I_0(\lambda)}{I(\lambda)} \right) = \sigma(\lambda) \cdot c \cdot L. \quad (1.2)$$

In a laboratory setting, Eq. (1.1) or (1.2) can be used to directly calculate an absorber's concentration, provided there is knowledge of its cross section. In the open atmosphere, however, absorption spectroscopy techniques are far more complex. On one hand, $I_0(\lambda)$ is not accessible since we measure from inside the medium we want to measure. On the other hand, there are several environmental and instrumental effects that influence measurement results. These effects include the following [23].

- Rayleigh scattering is due to small molecules present in the atmosphere and is heavily influenced by wavelength (hence the blue colour of the sky).
- Mie scattering is caused by particles and larger molecules suspended in the atmosphere and is not very dependent on the wavelength (hence the white colour of clouds).
- Instrumental and turbulence effects are the instrument's transmissivity and atmospheric turbulence in the optical path also limit light intensity.

In addition, we also have to take into account that, in the atmosphere, there are a number of trace gases that interfere with passing light. Another aspect worth mentioning is that our device is never pointed directly at the light source (the Sun) but always processes light that has been scattered at some unknown point in the optical path. This means that the light that reaches our detector is only the scattered fraction of the sunlight, depending on the system's position and geometry, as well as wavelength. The expansion of Lambert–Beer's equation to include all these effects results in Eq. (1.3).

$$\begin{aligned} \epsilon_{TG}(\lambda, s) &= \sum_i \sigma_i(\lambda, s) \cdot c_i(s) \\ I(\lambda) &= I_0(\lambda) \cdot A(\lambda, \dots) \cdot S(\lambda) \cdot \\ &\quad \cdot \exp \left[- \int [\epsilon_{TG}(\lambda, s) + \epsilon_M(\lambda, s) + \epsilon_R(\lambda, s)] ds \right] \end{aligned} \quad (1.3)$$

Where $A(\lambda, \dots)$ is the fraction of scattered light that reaches the device, $S(\lambda)$ represents instrumental and turbulence effects, $\sigma_i(\lambda, s)$ is the absorption cross section of absorber i , c_i is the concentration of absorber i . $\epsilon_{TG}(\lambda, s)$ is the absorption by the i trace gases, $\epsilon_R(\lambda, s)$ represents Rayleigh's extinction coefficient and $\epsilon_M(\lambda, s)$ represents Mie's extinction coefficient. The interest of this equation lies within the retrieval of c_i , a given absorber's concentration. Since the integral is taken along the total atmospheric path of the measured photons, and considering that their cross sections do not vary significantly in atmospheric conditions, it is possible to define the concept of slant column, which is of great importance [22].

$$SC_i = \int c_i(s) ds \quad (1.4)$$

This quantity, as Eq. (1.4) shows, equals the integral of an individual absorber's concentration along the atmospheric optical path of relevance. Now, without knowledge of $I_0(\lambda)$, these equations cannot give us absolute concentration values. We can, however, use another scattered light spectrum as reference in Eq. (1.2). Instead of

absolute densities, this will yield relative changes in the atmosphere. We thus arrive at Eq. (1.5).

$$\begin{aligned} \ln\left(\frac{I_{\text{ref}}}{I}(\lambda)\right) &= \ln\left(\frac{A_{\text{ref}}}{A}(\lambda, \dots)\right) + \ln\left(\frac{S_{\text{ref}}}{S}(\lambda)\right) \\ &\quad + \sum_i (\sigma_i(\lambda) \cdot \Delta \text{SC}_i(\lambda)) + \Delta \tau_M(\lambda) \end{aligned}$$

Where ΔSC_i is the relative slant column of absorber i ; $\Delta \tau_M$ is the relative Mie scattering term, integrated to its optical thickness; and $\Delta \tau_R$ is the relative Rayleigh scattering term, integrated to its optical thickness. This is where the principle of DOAS is applied. Instrument features, scattering and other atmospheric effects have broad absorption spectral profiles, which vary slowly with wavelength. Several trace absorbers have narrow and rapidly varying spectral signatures in at least a small section of the spectrum. By using Eq. (1.5), we can separate these contributions [11].

$$\sigma(\lambda) = \sigma'(\lambda) + \sigma_0(\lambda) \quad (1.5)$$

Here, the broad part of the optical thickness ($\sigma_0(\lambda)$) can be separated from the narrow part ($\sigma'(\lambda)$ – differential) by approximating it by a low-order polynomial, resulting in Eq. (1.6).

$$\ln\left(\frac{I_{\text{ref}}}{I}(\lambda)\right) = \sum_{i=1}^n \sigma'_i(\lambda) \cdot \Delta \text{SC}_i + \sum_{j=0}^m a_j \cdot \lambda^j \quad (1.6)$$

Where $\sum_{i=1}^n \sigma'_i(\lambda) \cdot \Delta \text{SC}_i$ is the differential part (narrowband, rapidly varying with wavelength) and $\sum_{j=0}^m a_j \cdot \lambda^j$ is a low-order polynomial, used to remove the broadband spectral features resulting from atmospheric and instrumental phenomena.

In practice, the mathematical solving of Eq. (1.6) is not enough since it does not account for the Ring effect or the non-linearities that result from stray light and wavelength shift in measured and cross-section spectra.

The Ring effect is a consequence of rotational Raman scattering: molecules in the atmosphere do not absorb photons in a purely elastic (Rayleigh scattering) fashion. A small portion of the light–matter interaction is in fact inelastic [5, 22]. This changes the light source frequencies as seen from the detector. This phenomenon was first noticed by Grainger and Ring in 1962. At the time, they noticed that the well-known Fraunhofer lines would slightly change when one observed them by using moonlight instead of scattered daylight [14]. Mathematically, the Ring effect is introduced into the DOAS expressions as a synthetically produced pseudo-absorber.

Up until this point, the DOAS problem can be solved by a system of linear equations of the form displayed in Equation 1.7.

$$\tau = A \cdot X \quad (1.7)$$

A is an $m \times n$ matrix. Its columns are the differential cross-sections for the measurement target gas, $\sigma'_i(\lambda)$, and the wavelength powers ($\lambda, \lambda^2, \lambda^3, \dots$) according to the polynomial used for the broadband extraction described above, $P(\lambda) = \sum_{j=0}^m a_j \lambda^j$. The lines of matrix A are the wavelength window of study, as seen by the spectrometer

used in the experiment. This leads to there being many more lines than columns in A . The system is thus overdetermined. Solving it requires the use of numerical approximations, and the most common approach is a least-squares approximation, in which the best solution minimises $\chi^2 = [\tau - A \cdot X] [\tau - A \cdot X]^T$. The upper script T used in this expression denotes the transpose of the preceding matrix [22, 23].

A crude DOAS algorithm might not go any forward. In effect, this is precisely the approached followed in [31] for smoke detection using machine learning techniques. A more refined measurement, aimed at quantification of the target trace gases and not at determining the presence of a particular type of atmospheric event requires an additional consideration, and some more algorithmic steps. There are in fact some non-linearities in the complete retrieval process. These non-linearities are not retrievable through linear algorithms alone. These non-linear effects present themselves as shifts, stretches and offsets in the measured signal. They do not directly change the dependent variable values (i.e., the radiance), but instead "move" the scale of the independent variable (i.e., the wavelength). Therefore, linear approximations such as least-squares minimisation are not sensitive to them. A non-linear approximation algorithm such as Levenberg–Marquardt [24] can be used, and the expression that is being solved is presented in Equation 1.8.

$$\ln \left(\frac{I_{\text{ref}}(\lambda)}{I(\lambda + \text{shift}) + \text{o_set}} \right) = \sum_{i=1}^n \sigma_i'(\lambda) \cdot \Delta \text{SC}_i + \sum_{j=0}^m a_j \cdot \lambda^j \quad (1.8)$$

Programming-wise, solving these equations is an iterative two-stage process, which runs until one of the following typical stop criteria are met.

Maximum iteration number: This is a self-explanatory criterion. It limits the number of times the algorithm's cycle can run;

Minimum improvement threshold: As the algorithm proceeds, this criterion ensures that it progresses in the correct direction, i.e., minimising χ^2 ;

Minimisation target: If χ^2 becomes lower than this given threshold, the cycle is terminated.

The cycle begins by the determination of the concentration values of the target trace gases and the χ^2 score is calculated. The wavelength window is shifted, stretched and offset according to the initial conditions. The χ^2 is re-calculated and compared to the previous value. This cycle is iteratively repeated in the best minimisation direction until any of the stop criteria are met and the cycle is terminated. The algorithm is illustrated (simplified) in Figure 1.5.

1.3.1 Types of DOAS experiments

There are two main families of DOAS assemblies, with different goals and capabilities:

- Active systems, of which a simple illustration is presented in Fig. 1.6, are characterized by relying on an artificial light source for their measurements. A spectrometer at the end of the light path performs spectroscopic detection. Active

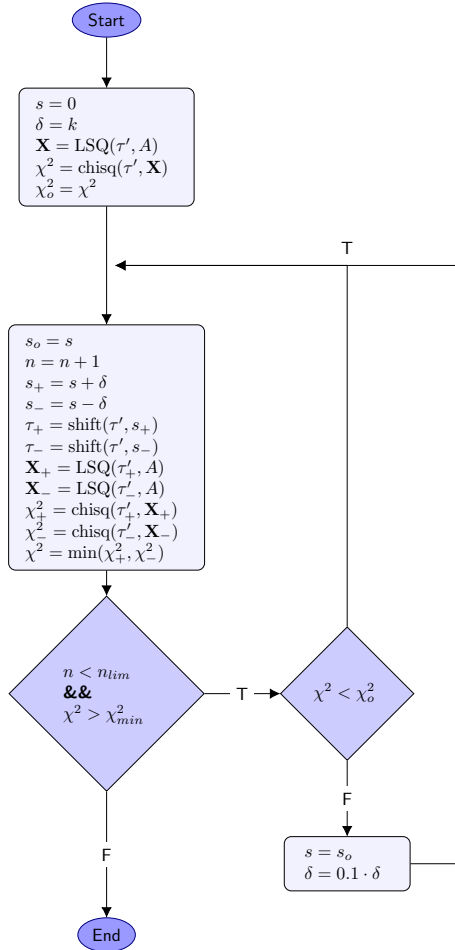


Figure 1.5: Simplified schematic flowchart of the DOAS algorithm, including the non-linear part.

DOAS techniques are very similar to traditional in-lab absorption spectroscopy techniques [23];

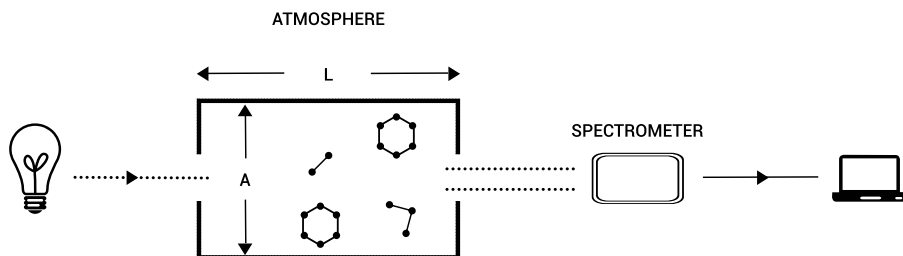


Figure 1.6: Active DOAS schematic.

- Passive DOAS techniques, illustrated in Fig. 1.7, use natural light sources, such as the Sun and the moon, in their measurement process. An optical system is pointed in certain elevation and azimuth angles and sends the captured light into a spectrometer, connected to a computer. The system returns the total value of the light absorption in its path [23, 22].

Within the two main DOAS families, there are several types of possible experiment.

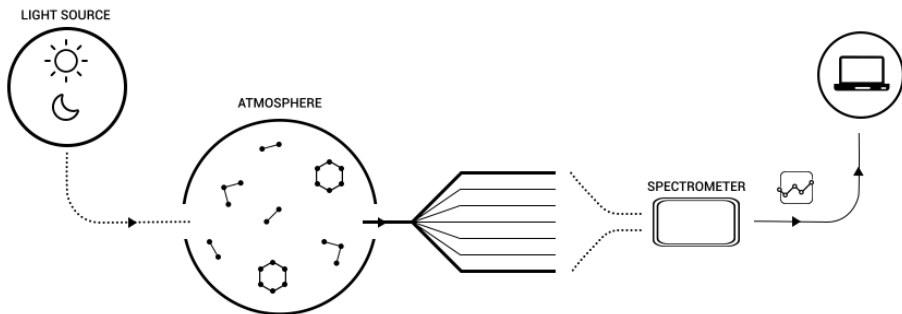


Figure 1.7: Passive DOAS schematic.

Differences in the design of these assemblies originate from a number of different target requirements. Active or passive applications can differ with relation to their intended spectral range, light throughput or resolution, among others.

In active experiments, the choice of the light source is the most critical aspect of the whole experimental design. Active DOAS light sources must be stable, have a very high throughput (these experiments are often conducted over long optical paths) and must have an adequate cost to purchase, maintain and operate. This is especially true in long-running experiments, which must remain working for months or even years. Moreover, the spectral range of the emitted light is also of central importance, because most trace gases have very particular spectral cross sections. The spectral structure of the emitted light is also an important feature to consider, for similar reasons.

The sun and the moon are the two most important light sources when it comes to passive DOAS applications. Sunlight can be used directly or after a scattering event, the latter being the more common. In these experiments, instead of pointing directly at the sun, the collector is pointed at a certain point in the atmosphere, entering the system after it has been scattered. There are many possible geometries to a scattered sunlight DOAS experiment. Some of them are schematically represented in Figure 1.8.

Although instrumentally simpler than their active counterpart, passive DOAS applications require more care in the retrieval process. In this kind of application, light sources are extremely far away. Additionally, they are normally highly structured. This means that one has to be extremely mindful when using it for the retrieval of small concentration changes. In addition to this, there is always the need to convert the system's direct measurement, a column density, into vertical densities. Since in scattered sunlight measurements, the optical path is impossible to calculate in a precise manner, this requires the use of complex radiative transfer models [23, 13].

1.3.1.1 Satellite Measurements

One particularly interesting use of passive DOAS are satellite measurements. There are three types satellite DOAS experiments:

Occultation measurements: this is a direct sunlight measurement. Light comes from the sun and traverses the Earth's atmosphere in a tangential manner before entering the satellite's light collector;

Limb: a scattered sunlight measurement, in which the collector is pointed towards

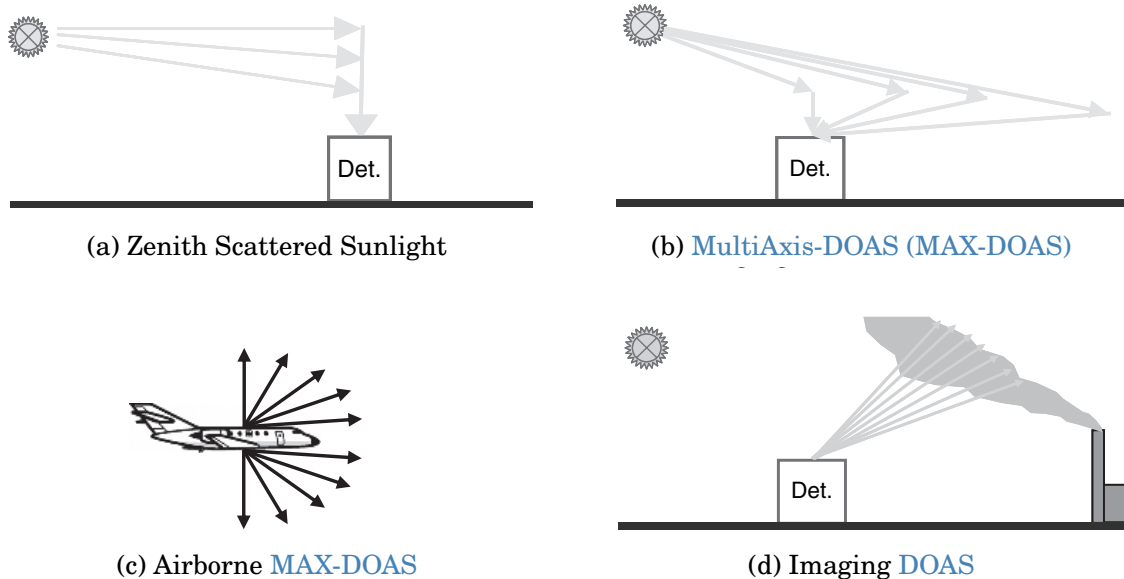


Figure 1.8: Several examples of possible passive DOAS experiment geometries. All these examples use only the light from an astronomical source to detect many atmospheric trace gases. All these examples were taken from [23].



Figure 1.9: Occultation measurement schematic representation [23]

the Earth, at an angle. Light reaches the detector after being scattered in the atmosphere, the ground, or both;

Nadir: this is the most common measurement geometry for satellite experiments. In this mode, light that gets reflected off the Earth's surface is captured by the collecting device, while it is pointing directly down.

Satellite based DOAS measurements have also been important because they have given rise to new trace gas retrieval techniques. Through them, new trace gases, previously unreachable through DOAS have been quantified on a global level, such as carbon monoxide through Weighting Function Modified Differential Optical Absorption Spectroscopy (WFM-DOAS) [9, 8].

WFM-DOAS is a trace gas column retrieval algorithm, developed in the beginning of the 21st century, with the main goal of determining the total columns of gases such as Carbon Monoxide (CO), Water (H_2O) or Carbon Dioxide (CO_2) from satellite nadir data [8]. Instead of using literature-obtained cross-section data for each target trace gas, the WFM-DOAS approach uses weighing functions, calculated through the application of a radiative transfer model, such as SCIATRAN [26]. Still, the retrieval

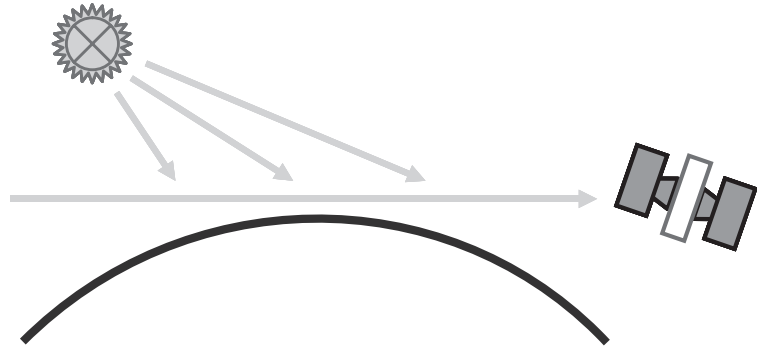


Figure 1.10: Schematic representation of the limb satellite measurement geometry.

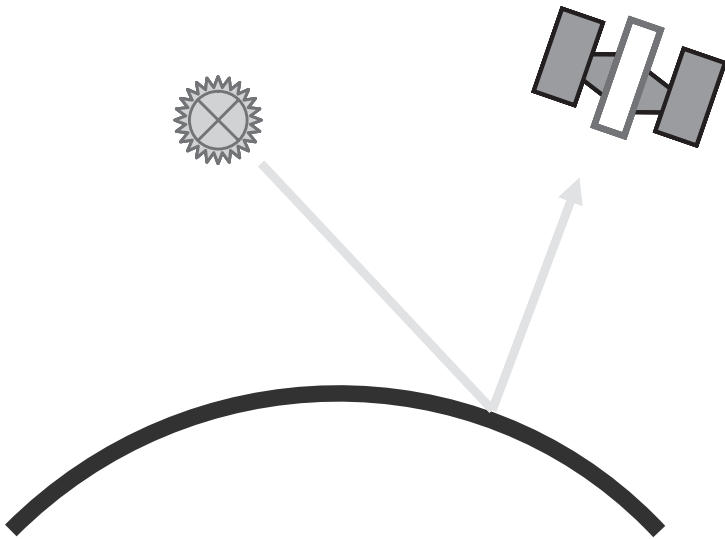


Figure 1.11: Schematic representation of the nadir satellite measurement geometry.

is based on a fitting process. Equation 1.9, adapted from [9, 8] can be called the **WFM-DOAS** equation.

$$\left\| \ln I_i^{obs}(\mathbf{V}^t) - \left[\ln I_i^{mod}(\bar{\mathbf{V}}) + \sum_{j=1}^J \frac{\partial \ln I_i^{mod}}{\partial V_j} \Bigg|_{\bar{V}_j} (\hat{V}_j - \bar{V}_j) + P_i(a_m) \right] \right\|^2 = \|RES\|^2 \rightarrow \min \quad (1.9)$$

In Equation 1.9, I_i^{obs} is the observed sun-normalised radiance (the ratio between a nadir radiance measurement and solar irradiance) for the center wavelength λ_i of detector pixel number i . \mathbf{V} are the vector that have vertical columns as their components. These can be true, V^t , modelled, \bar{V}_j , or approximated, \hat{V}_j . The true columns are unknown as we only have the radiance value and not the things on which it depends, modelled vertical columns are taken from the literature (they are climatological values) and \hat{V}_j are one of the fitting parameters. The other being a_m , the low order polynomial (P) coefficients. RES is the fit residuum, which is minimised for the fitting.

1.4 Important Notes on DOAS in practice

Theoretically, the procedure described in Section 1.3 would be enough to obtain the target trace gas concentrations. In practice, this is an over-simplification. There are several additional required steps, most of them concerning a certain conditioning that one has to apply to both the collected and literature spectral signals.

1.4.1 Cross section conditioning

Unless conditions are absolutely stable, and one is able to record all data with the same device, which is impractical to the point of infeasibility, external literary sources are required for the DOAS analysis. These data are obtained with standardised trace gas sampling, extremely high resolution spectrometers and in carefully designed laboratory experimental setups.

To use external cross sections in one's own experiments, these data must be adapted to one's equipments. The very high resolution spectra coming from the literature are convolved with the instrument function of the real experiment's spectrometer. This function can be thought of as the device's impulse response. Since the spectrometer is inevitably imperfect, this response is not nearly as sharp as the impulse itself, and is normally modelled as a Gaussian curve fitted to a known source's well defined, impulse-like narrow structures. An Hg-Cd lamp was used in Merlaud's 2013 work, for instance [22]. For most spectrometers, this step is not actually required, as manufacturers already provide a very accurate spectral resolution value.

After calculating or fetching this value from the device's manual, it is a matter of creating a Gaussian kernel that can be used to filter the high resolution spectra through convolution. The **Full Width at Half Maximum (FWHM)** of the Gaussian kernel is equal to the spectrometer's resolution. One can ensure this by using the formula in Equation 1.10 which relates the width of the kernel with the standard deviation used to create it. The signal that results from the convolution of the literature cross sections and the gaussian kernel can be thought of as how the cross section would look if it had been acquired using the experiment's spectrometer.

$$FWHM = 2\sqrt{2\sigma^2 \ln 2} \rightarrow FWHM \approx 2.355 \cdot \sigma \quad (1.10)$$

The final step in this process of conditioning high resolution literature cross sections to the experiment that one is conducting is the discretisation of this signal. Physically, spectra are continuous signals. In practice, they were all captured using finite-resolution devices, and therefore are a digital signal. However, the resolution of the literature cross sections is so high in comparison to the usual resolution of a DOAS experiment spectrometer that one can think of this signal as being *quasi-continuous*. In order for them to be used in DOAS calculations, they have to be "re-discretised" onto the experiment's spectrometer sensor resolution. Since it is seldom the case (if ever) that the literature and the low resolution pixels coincide, a mathematical routine is used to interpolate the former onto the latter. The most commonly used routine is the cubic spline interpolation, widely regarded as the best compromise between computational expense and accuracy [4]. Overall, cross sections used in DOAS undergo a process illustrated in Figure 1.12 [11, 4].

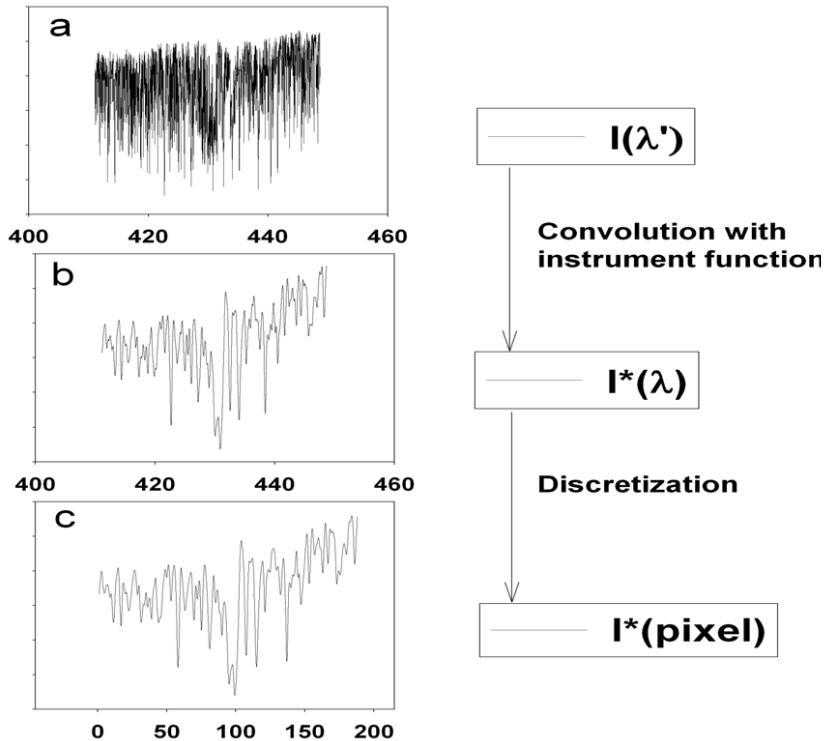


Figure 1.12: Before being used in DOAS calculations, literature trace gas cross section spectra must undergo a conditioning process to make sure they are compatible with the current experiment's instruments. Figure adapted from [4]

1.4.2 Spectral Calibration

One other small but important correction that can bias results is the lack of proper calibration between cross sections and collected spectra. Figure 1.13 shows how a conditioned cross section present slight wavelength related discrepancies.

These small nonconformities are caused not only because both types of data were captured by different spectrometers, but also because conditions most certainly changed. This means that situations in which calibration must be handled with care are the norm. This is done by running an iterative process that makes slight adjustments to the function mapping wavelength to pixel number, as explained in the next few paragraphs.

The light that enters the spectrometer is scattered by the diffraction grating before reaching the device's sensor, which is divided into pixels. These pixels have a well defined and finite width. At the centre of each one of them, the signal's intensity can be described by Equation 1.11, in which I is the intensity, i the pixel number and λ the wavelength.

$$I(i) = \int_{\lambda(i)}^{\lambda(i+1)} I(\lambda) d\lambda \quad (1.11)$$

The expression in Equation 1.11 assumes that the signal has been conditioned properly, as described in Section 1.4.1, through the convolution of the cross section

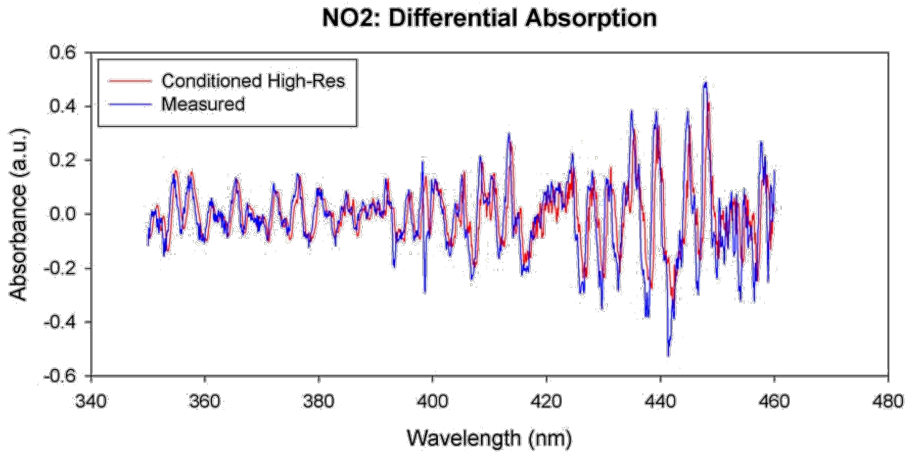


Figure 1.13: This figure, taken from [4], shows the difference between NO_2 cross sections. The red line comes from the literature, and has been conditioned to the experiment spectrometer. The blue line was actually collected with that device. The slight discrepancies that can be observed are calibration defects.

data with the instrument function and adequate discretisation. The smaller $\Delta\lambda = \lambda(i+1) - \lambda(i)$, the finer the instrument's resolution. This is, of course, inherent to the system and cannot be changed. What can and should be changed during analysis is the central wavelength assigned to each pixel. This assignment is in fact what constitutes the instrument's calibration.

The most common way of conducting said calibration is by introducing a polynomial describing wavelength to pixel relationship. This polynomial is the wavelength-pixel mapping function, and can be written as in Equation 1.12.

$$\lambda(i) = \sum_{k=0}^q \gamma_k \cdot i^k \quad (1.12)$$

In Equation 1.12, γ_k determines how the pixels are mapped to the wavelength (λ), and the type of mapping effect depends on k . Changing γ_0 shifts the signal left or right; changing γ_1 introduces linear distortions to the pixel mapping, i.e., stretching or squeezing of the signal. One can fit this polynomial up towards $k = \infty$, in theory, but normal spectrometer calibrations are only run up to the second or third degree. The Avantes spectrometers that were used in this dissertation are factory-calibrated to a fourth order polynomial.

The non-linear portion of the DOAS algorithm, described in Section 1.3, is indeed a wavelength calibration. However, it is important to previously calibrate every spectral signal before actually running the DOAS fitting process. This is because the types of optimisation algorithm used in this technique, such as Levenberg–Marquardt, tend to find local minima or to not converge if there is significant misalignment between the spectra.

For passive applications using the sun as the light source, one can use a high resolution solar spectrum (see Figure 1.14), and the Fraunhofer bands in it (which have a very well defined wavelength that can be used as ground truth) to align the various spectra. For active applications, one can use the light source's own spectrum, either

provided by the manufacturer or previously collected in the absence of atmospheric or other effects.

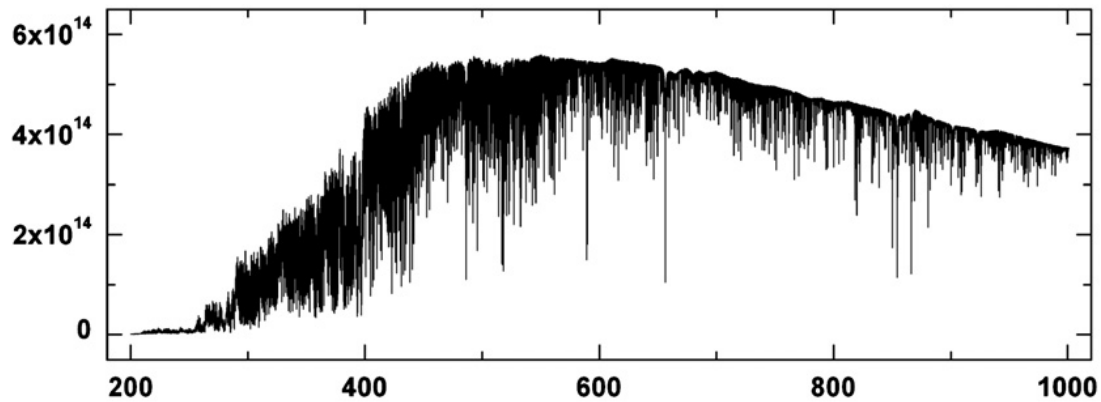


Figure 1.14: High resolution solar spectrum commonly used to calibrate the various spectral signals in DOAS experiments [10].

1.5 Tomographic algorithms and reconstruction techniques

Tomography is the cross-sectional imaging of an object through the use of transmitted or reflected waves, captured by the object exposure to the waves from a set of known angles. It has many different applications in science, industry, and most prominently, medicine. Since the invention of the Computed Tomography ([Computed Tomography \(CT\)](#)) machine in 1972, by Hounsfield [15], tomographic imaging techniques have had a revolutionary impact, allowing doctors to see inside their patients, without having to subject them to more invasive procedures [20].

The central thought around tomographic image reconstruction is to recreate the information contained inside a target physical body, without having to cut it or open it in any way. The theory is based on Radon's idea that it is possible to "*represent a function written in \mathbb{R} in the space of straight lines (\mathbb{L}) through its line integrals*" [25].

Say we have a body that we want to fully characterise without cutting open or destroying in any way. Now imagine we can traverse it with some kind of radiation, ray by ray, and that we are able to measure the rays after they traverse the target. What we would capture would be relative to the emitted radiation, of course, but it would also contain information on how that ray had interacted with the target body's matter. In the case of the ubiquitously used X-Ray radiation, the measurement would be one of the total attenuation "imprinted" onto the ray by the target body's molecules, in the ray's particular direction. If said body is heterogeneous, the total attenuation can be derived by the infinitesimal sum of all different attenuation phenomena caused by the object's several different constituents (the same can be said of a homogeneous object, but in that case there is only one type of attenuation present). This means that each one of the rays contains information regarding the constitution of said body.

The question that arises is thus "*how we can use this information to create a spatially accurate representation of this target's interior composition?*". The answer to this

1.5. TOMOGRAPHIC ALGORITHMS AND RECONSTRUCTION TECHNIQUES

question lies on many factors, but the most prominent of which are surely choosing the quantity that we are trying to find (that characterises the object) and assembling the projections (that is what we call the line integrals in tomographic imaging) in a way that allows solving an equation system for the aforementioned quantity. This assembly, a matrix of projections organised by their angles and position within the detector, is called sinogram. All tomography methods revolve around finding the relationship between it and the system's geometrical description [7, 20, 19, 17, 18, 12].

Let's consider the case in which we deal with a single ray of solar light entering the atmosphere at a given point. Since the atmosphere contains numerous absorbers and comparable atmospheric effects, the ray changes from the point where it enters the atmosphere to the point at which it is measured by a detector. Total absorption will depend on the pollutant species, their cross-section and their concentration, since it obeys Lambert-Beer's law. Looking from another angle, this absorption is also the line integral that we will use to reconstruct our image. With DOAS, it is possible to measure several pollutants at the same time, but for simplicity (and since it is one of the most studied compounds in the field), let's consider that the single pollutant in our atmospheric mixture is NO₂.

The problem of tomographic reconstruction can be approached in a number of ways, depending mostly on the authors. In my literary search, I have found that Kak and Slaney [20] have certainly explained this problem in one of the clearer ways available. Therefore, I shall base the rest of my presentation in their writings, and complement with other authors' notes wherever necessary.

Considering the coordinate system displayed in Figure 1.15. In this schematic, the object is represented by the function $f(x, y)$. The (θ, t) parameters can be used to define any line in this schematic. Line AB in particular can be written:

$$x \cdot \cos(\theta) + y \cdot \sin(\theta) = t \quad (1.13)$$

And if we were to write a line integral along this line, it would look like Equation 1.14, the Radon transform of function $f(x, y)$:

$$P_\theta(t) = \int_{-\infty}^{\infty} f(x, y) \cdot \delta(x \cdot \cos(\theta) + y \cdot \sin(\theta) - t) dx dy \quad (1.14)$$

Where δ , the delta function, is defined in Equation 1.15.

$$\delta(\phi) = \begin{cases} 1, & \phi = 0 \\ 0, & \text{otherwise} \end{cases} \quad (1.15)$$

As I have mentioned previously, a projection is a set of line integrals such as $P_\theta(t)$. Geometry plays a very important role in how the integrals are written and solved for reconstruction. The simplest case is the one where the set is acquired in a row, describing what is called a parallel geometry. Another more complex case is when a single point source is used as origin for all rays, forming a fan. This is called a fan-beam array. There are other possible geometries, but they fall out of the scope of this work and will therefore not be addressed any further.

The Fourier Slice Theorem (FST) is the most important component of the most important algorithm in tomographic inversion, the Filtered BackProjection algorithm

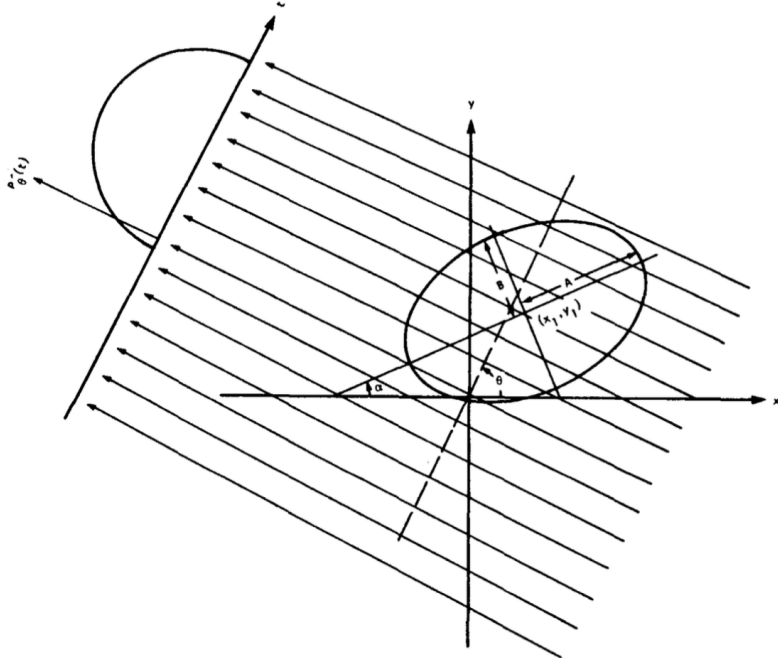


Figure 1.15: Schematic representation for coordinate setting. The image depicts a parallel projection setting [21].

([Filtered BackProjection \(FBP\)](#)). [FST](#) is based on the equality relation between the two-dimensional Fourier Transform ([Fourier Transform \(FT\)](#)) of the object function and the one-dimensional [FT](#) of the object's projection at an angle θ . Let's start by writing the [2D FT](#) for the object function, [Equation 1.16](#), and the [1D FT](#) of projection P_θ , in [Equation 1.17](#).

$$F(u, v) = \int_{-\infty}^{\infty} \int_{-\infty}^{\infty} f(x, y) \cdot \exp [-j2\pi(ux + vy)] dx dy \quad (1.16)$$

$$S_\theta(\omega) = \int_{-\infty}^{\infty} P_\theta \cdot \exp [-j2\pi\omega t] \quad (1.17)$$

For simplicity, let's consider the [2D FT](#) at the line defined by $v = 0$ in the frequency domain. We rewrite the [2D FT](#) integral as:

$$F(u, 0) = \int_{-\infty}^{\infty} \int_{-\infty}^{\infty} f(x, y) \cdot \exp [-j2\pi\omega ux] dx dy \quad (1.18)$$

Notice that y is not present in the phase factor of the [FT](#) expression anymore, and this means we can rearrange the integral as:

$$F(u, 0) = \int_{-\infty}^{\infty} \left[\int_{-\infty}^{\infty} \mathbf{f}(\mathbf{x}, \mathbf{y}) d\mathbf{y} \right] \cdot \exp [-j2\pi\omega ux] dx \quad (1.19)$$

Now, the **bold** part of [Equation 1.19](#) is similar to [Equation 1.14](#). It is precisely that equation, considering $\theta = 0$ and a constant value of x , as in [Equation 1.20](#).

$$P_{\theta=0}(x) = \int_{-\infty}^{\infty} f(x, y) dy \quad (1.20)$$

1.5. TOMOGRAPHIC ALGORITHMS AND RECONSTRUCTION TECHNIQUES

This in turn can be substituted in Equation 1.19, finally arriving at:

$$F(u, 0) = \int_{-\infty}^{\infty} P_{\theta=0}(x) \cdot \exp [-j2\pi ux] dx \quad (1.21)$$

And this is the one-dimensional **FT** for the projection at angle $\theta = 0$. Finally, the enunciation of the Fourier Slice Theorem:

The Fourier Transform of a parallel projection of an image $f(x, y)$ taken at angle θ gives a slice of the two-dimensional Fourier Transform, $F(u, v)$, subtending an angle θ with the u -axis (see Figure 1.16)

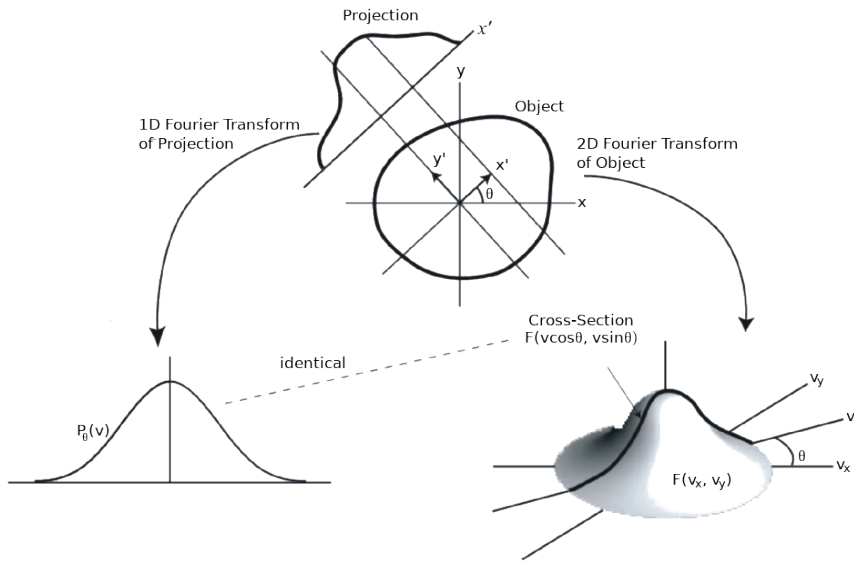


Figure 1.16: The **FST**, a schematic representation [2].

If one takes the **FST** into account, the idea behind the **FBP** seems to appear almost naturally. Say one has a single projection and its Fourier transform. From the **FST**, this projection is the same as the object's two-dimensional **FT** in a single line. A crude reconstruction of the original object would result if someone were to place this projection in its right place in the Fourier domain and then perform a two-dimensional **Inverse Fourier Transform (IFT)**, while assuming every other projection to be 0. The result, in the image space, would be as if someone had smeared the object in the projections direction.

What is really needed for a correct reconstruction is to do this many times, with many projections. This brings a problem with the method: smearing the object in all directions will clearly produce a wrong *accumulation* in the center of the image, since every projection passes through the middle (remember we are still talking about parallel geometry projections) and are summed on top of each other, but on the outer edges, this does not occur. If one does not address this, the image intensity levels in the reconstructed image will be severely overestimated in the center and underestimated in the edges (due to normalization). The solution is conceptually easy: we multiply the Fourier transform by a weighting filter proportional to its frequency (ω)

and that encompasses its relevance in the global scheme of projections. If there are K projections, then it is adequate for this value to be $\frac{2\pi|\omega|}{K}$. As an algorithm, **FBP** can be written as in Algorithm 1.

Algorithm 1: The Filtered BackProjection Algorithm

Result: A reconstructed image of the projected object.

```

for  $\theta \leftarrow 0$  to  $180$  by  $\frac{180}{K}$  do
    measure projection  $P_{theta}(t)$ ;
    FT( $P_{theta}(t)$ ), rendering  $S_{theta}(\omega)$ ;
    Multiply by  $\frac{2\pi|\omega|}{K}$ ;
    Sum the IFT of the result in the image space;
end
```

Parallel projections, in which the object is scanned linearly from multiple directions, have the advantage of having a relatively simple reconstruction scheme. However, they usually result in acquisition times which are in the order of minutes. A faster way of collecting the data is one where all radiation emanates from a single point-source, which rotates around the target object (as well as the detectors). There are two types of fan-beam projections: equiangular and equally spaced. In this project, I have only worked with equiangular processes, so I will not include an explanation for equally spaced fan-beam projections. The reader may find this well described (much better than I would be able to) in [20] and [19].

Consider Figure 1.17. If our projection data were acquired through a parallel ray geometry, we would be able to say that ray SA belonged to a projection $P_{theta}(t)$, in which θ and t would be written:

$$\theta = \beta + \gamma \quad \text{and} \quad t = D \cdot \sin \gamma \quad (1.22)$$

In Equation 1.22, D is the distance between the source S and the origin O ; γ is the angle of a ray within a fan and β is the angle that the source S makes with a reference axis. Through these relationships one can *translate* the parallel projection's **FBP** algorithm to the fan-beam case, which involves several complex geometric transformations, although the overall rationale is exactly the same.

Another particularity of fan-beam projection data is the fact that they can be sorted into a parallel projection. For that, one starts with the premise that if one were to substitute the fan geometry for parallel beams, most of the fan-beam rays would also appear in some projection of the parallel setup. This re-sorting algorithm starts with Equation 1.22. Now, if we call a fan-beam projection taken at angle β $R_\beta(\gamma)$, and a parallel projection taken at angle θ $P_\theta(t)$, one could thus write Equation 1.23, which can already be used to re-sort any fan-beam projection into parallel beam geometry.

$$R_\beta(\gamma) = P_{\beta+\gamma}(D \cdot \sin \gamma) \quad (1.23)$$

The angular interval between fan-beam projections can be written $\delta\beta$, and the angular interval of rays within each fan is written $\delta\gamma$. In the case that they are the same ($\beta = \gamma = \alpha$), then it is the case that they can both be replaced by multiples of that interval in Equation 1.23, which becomes Equation 1.24.

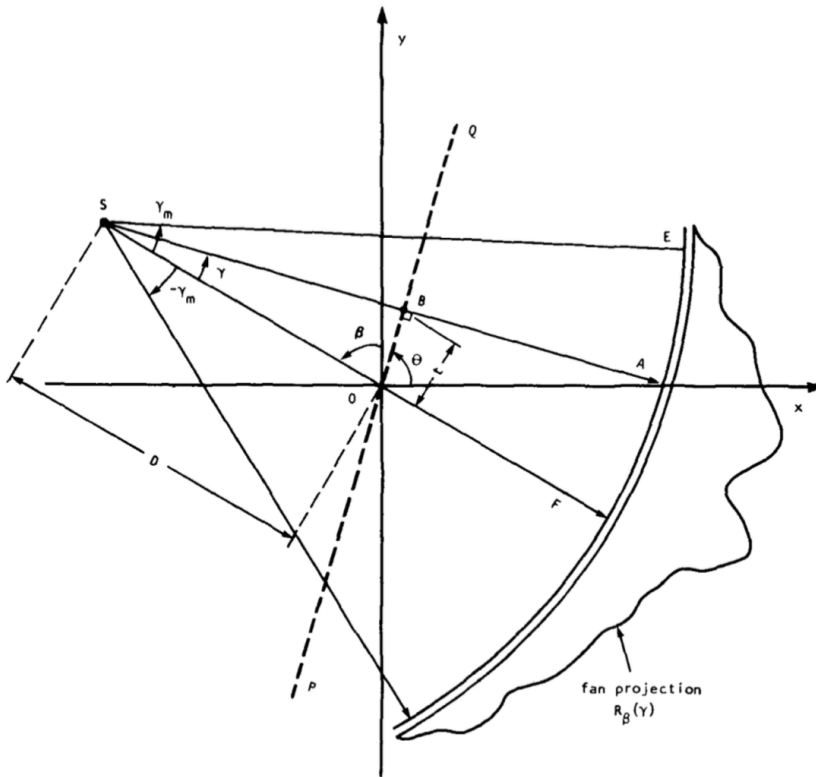


Figure 1.17: Schematic representation of an equiangular fan-beam projection, taken from [20].

$$R_{m \cdot \alpha}(n \cdot \alpha) = P_{m \cdot \alpha+n \cdot \alpha}(D \cdot \sin n \cdot \alpha) \quad (1.24)$$

Or, in non-mathematical notation, the n^{th} ray of the m^{th} radial projection (R) is the same as the n^{th} ray in the $(m+n)^{\text{th}}$ parallel projection. Although being much simpler than directly applying the [FBP](#) algorithm to the fan-beam projection data, this method has a limitation, which is the non-uniformity of the generated parallel projections. This can usually be corrected through interpolation [21].

1.5.1 Iterative Tomographic Reconstruction Methods

This subsection borrows heavily from an article I published in 2021, in which I described the tomographic part of this thesis [30].

Iterative reconstruction algorithms are based on simpler premises than [FBP](#), but they do require a more computational approach. One can start by thinking that a certain tomographic problem is modelled by its sinogram, which is the set of all projections that were gathered by the sensors. The sinogram is a matrix whose columns represent the sensor that gathered the information and whose lines represent the projection number. The resulting image can also be thought of as a matrix. Each value of this matrix corresponds to a pixel intensity, which gives it its intensity and/or colour. The third matrix is the system matrix. This matrix stores the length of each ray in each projection contained in one of the image's pixels. These lengths are obtained through a process called discretisation. One of the most famous and studied

algorithms for this purpose (and the one I ended up using for this work), the Siddon algorithm, is described some paragraphs ahead, in Section 1.5.2.

Iterative methods attempt to solve the relationship between these three matrices, which is presented in Equation 1.25. In it, $\mathbf{g} \in \mathbb{R}^{m,1}$ is the column vector sinogram, $\mathbf{a} \in \mathbb{R}^{m,n}$ is the system matrix and $\mathbf{f} \in \mathbb{R}^{n,1}$ is the column vector image. m is the number of measurements (projections times detectors) and n is the number of pixels in the image. As their designation implies, iterative algorithms produce an estimation for \mathbf{f} which is updated in the direction of error minimisation in every iteration [20, 7].

$$\mathbf{g} = \mathbf{a} \cdot \mathbf{f} \quad (1.25)$$

The popularity of algebraic reconstruction methods has not remained constant throughout the years. For a long time, they have been considered too computationally intensive to use in a clinical setting (paradoxically, Hounsfield's machine used this kind of algorithm). This was in direct opposition to the fact that researchers know that these methods are better able to model reconstruction since Shepp and Vardi published the maximum likelihood tracer estimation in 1982. Nowadays, and since the mid nineties, these algorithms are the first choice whenever the reconstruction dataset is not too large to process using the available computational capabilities [12].

The general goal of iterative reconstruction algorithms is to solve Equation 1.25 [6]. In principle, any method that solves it can be used for image reconstruction in tomography. In reality, however, only a few are currently in use by the community. Of these, TomoSim uses two of the most prominent: Simultaneous algebraic Reconstruction Technique (SART) and Maximum Likelihood Expectation Maximisation (MLEM).

SART was presented in 1984 by Andersen and Kak [1] and the global idea is that the estimated image is corrected for all projections at the same time (in opposition to the original algebraic Reconstruction Technique, in which corrections were applied for each single projection). Iterations in SART change the estimated image according to Equation 1.26, iterating on k .

$$\mathbf{g}_i^{(k+1)} = \mathbf{g}_i^{(k)} + \frac{\sum_j \left[\mathbf{a}_{ij} \cdot \frac{\mathbf{p}_j - \mathbf{a}_j^T \cdot \mathbf{g}^{(k)}}{\sum_{i=1}^n \mathbf{a}_{ij}} \right]}{\sum_j \mathbf{a}_{ij}} \quad (1.26)$$

MLEM algorithms were first published in the medical imaging community in 1982, by Shepp and Vardi [27]. With this algorithm, image corrections are ruled by Equation 1.27, which also iterates over k .

$$\mathbf{f}_j^{k+1} = \frac{\mathbf{f}_j^k}{\sum_{i=1}^n \mathbf{a}_{ij}} \sum_{i=1}^n \frac{\mathbf{g}_i}{\sum_{j'=1}^m \mathbf{a}_{ij'} \mathbf{f}_{j'}^k} \quad (1.27)$$

This equation is very easy to implement computationally, if one observes that the sums of the second multiplication term expand neatly onto matrix products. In the end, this equation is the equivalent of writing Equation 1.28, as explained in [6], in which $\text{IMG}^{(k)}$ is the estimated image in the k^{th} iteration, NBP is the Normalised Backprojection operation, RSNG the real sinogram (as in coming from the detector hardware) and SSNG the simulated sinogram, calculated through the previous iteration.

$$\text{IMG}^{(k+1)} = \text{IMG}^{(k)} \times \text{NBP} \left(\frac{\text{RSNG}}{\text{SSNG}^{(k)}} \right) \quad (1.28)$$

1.5.2 Discretisation - The Siddon Algorithm

Discretisation is the process by which the **Region Of Interest (ROI)** is digitised into a computational platform. There are several algorithms designed for this effect that are available in the literature. One of the easiest to implement that is also adequate to this application (unsurprisingly) comes from the medical imaging field. It was published in 1985 by Robert Siddon [28].

The Siddon algorithm is one of the foremost path calculation algorithms in the medical field of radiology. It is not only used for the discretisation of tomographic fields, but also in the dose calculation process of radiation therapy patients. The idea behind the algorithm is that the total dose of a radiation ray, i.e., its path, is given by the sum of the length within each pixel that this ray traverses multiplied by the density of said pixel. In mathematical notation, one can write this as in Equation 1.29.

$$d = \sum_i \sum_j \sum_k kl(i, j, k) \cdot \rho(i, j, k) \quad (1.29)$$

In Equation 1.29, d is the radiological path (the projection value), i, j, k are the coordinate vectors, l is the length within a pixel and ρ is the pixel density. In our case, this last value is the trace gas column density for that pixel.

The main reason for Siddon's algorithm being easy to implement is its treatment of pixels (or voxels if in 3D). Instead of considering pixels as *atomic*¹ units, it defines them as the intersections of orthogonal sets of equally spaced lines (planes in 3D). Pixel lengths are determined by the looking at the intersections between the orthogonal lines and the radiation ray.

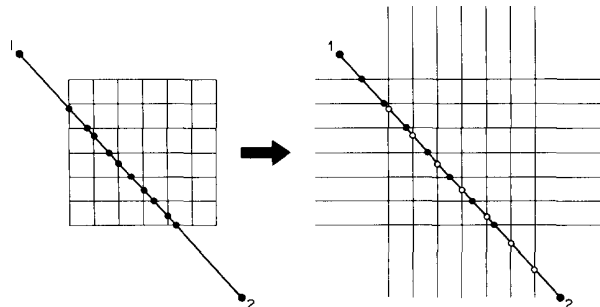


Figure 1.18: Grid and pixel definition, as they appear in the original article by Robert Siddon [28]. Pixels are "formed" by intersecting the ray (here going from point 1 to point 2) with the superimposed grid.

Since lines are orthogonal and equally spaced, all intersections can be calculated recursively after knowing where the first intersection is located. The calculation of

¹In their undivisible sense.

the radiologic path is achieved by determining the subset of the intersections between the orthogonal lines and the light ray that identifies individual pixels.

If $P_1 \rightarrow (X_1, Y_1)$ and $P_2 \rightarrow (X_2, Y_2)$ are the start and end of the radiologic path within the ROI, the line between them can be parametrically written as in Equation 1.30.

$$\begin{aligned} X(\alpha) &= X_1 + \alpha \cdot (X_2 - X_1) \\ Y(\alpha) &= Y_1 + \alpha \cdot (Y_2 - Y_1) \end{aligned} \quad (1.30)$$

In Equation 1.30, α is 0 at P_1 and 1 at point P_2 . Values of α within the ROI vary according to the positions of P_1 and P_2 with respect to the ROI. By determining α values of each intersection (in both directions), one can determine the length of the ray within the pixel by the difference of adjacent intersections. The whole algorithm can be written as in Algorithm 2.

Algorithm 2: Siddon's algorithm's procedural steps. After running this algorithm, one is able to represent any continuous ray through the analysis field as a sum of discrete lengths

Result: Discretised ROI space.

- calculate range of parametric values;
 - calculate range of pixel indices;
 - calculate parametric sets;
 - merge sets;
 - calculate pixel(or voxel) lengths;
 - calculate pixel indices;
-

Detailing the two-dimensional case² should start by the definition of the discretisation grid itself, as in Equation 1.31. The equation reflects the recursive nature of the grid definition. In it, d_x and d_y are the distances between the x and y planes, which correspond to the lengths of the pixels in those coordinates. N_x and N_y are the number of pixels in x and y that are contained in the grid.

$$\begin{aligned} X_{plane}(1) &= X_{plane}(1) + (i - 1) \cdot d_x \\ Y_{plane}(1) &= Y_{plane}(1) + (j - 1) \cdot d_y \end{aligned} \quad (1.31)$$

The parametric values α_{min} and α_{max} are given by the intersections of the ray with the sides of the grid ($i = 1$ and $i = N_x$) and can be written as in Equation 1.32.

$$\begin{aligned} \alpha_{min} &= \max \left\{ 0, \min [\alpha_x(1), \alpha_x(N_x)], \min [\alpha_y(1), \alpha_y(N_y)] \right\} \\ \alpha_{max} &= \min \left\{ 1, \max [\alpha_x(1), \alpha_x(N_x)], \max [\alpha_y(1), \alpha_y(N_x)] \right\} \end{aligned} \quad (1.32)$$

Not all line intersections have a corresponding parametric value. The ones that do are comprised within index ranges that are defined by Equation 1.33. This equation presents the case for the first coordinate (x), with the second coordinate having an identical expression.

²A three-dimensional case would be just the same but with an additional coordinate.

$$\begin{aligned} i_{min} &= N_x - \frac{X_{plane}(N_x) - \alpha_{min}(X_2 - X_1) - X_1}{d_x} \\ i_{max} &= 1 + \frac{X_1 + \alpha_{max}(X_2 - X_1) - X_{plane}(1)}{d_x} \end{aligned} \quad (1.33)$$

Equation 1.33 defines a range of possible indices for the pixels, in parametric fashion. We can use this range to construct the set of used parametric indices, given in Equation 1.34 for the x coordinate.

$$\{\alpha_x\} = \{\alpha_x(i_{min}), \dots, \alpha_x(i_{max})\} \quad (1.34)$$

Although Equation 1.34 only presents the expression for the first coordinate, there are similar expressions for the other coordinates at play. After determining the set of possible indices for x and y , these sets must be arranged in ascending order, creating an index superset. To this the minimum and maximum values, calculated in Equation 1.32, are appended. The resulting and final set of parametric values is presented in Equation 1.35.

$$\begin{aligned} \alpha^* &= merge(\alpha_x, \alpha_y) \\ \{\alpha\} &= \{\alpha_{min}, \alpha^*, \alpha_{max}\} \\ &= \alpha(0), \dots, \alpha(n) \end{aligned} \quad (1.35)$$

Where the last term, n , is given by the sum of all index range numbers, as in Equation 1.36, again for the two-dimensional case.

$$n = (i_{max} - i_{min} + 1) + (j_{max} - j_{min} + 1) \quad (1.36)$$

Each element of the array defined in Equation 1.35 is an intersection between the ray and a given pixel. Since they are ordered, it is possible to calculate the array of pixel lengths for each ray, using the expression in Equation 1.37.

$$l_m = d_{12}[\alpha(m) - \alpha(m - 1)] \quad (m = 1 \dots n) \quad (1.37)$$

With d_{12} being the distance between P_1 and P_2 , calculated through the Euclidean formula for distance between two points. In Tomosim, this distance is always equal to the trajectory's diameter.

Pixel $[i(m), j(m)]$ is located in the midpoint between the m^{th} and the $(m-1)^{\text{th}}$ intersections. It is given by the expression in Equation 1.38.

$$\begin{aligned} \alpha_{mid} &= \frac{\alpha(m) + \alpha(m - 1)}{2} \\ i(m) &= 1 + \frac{X_1 + \alpha_{mid} \cdot (X_2 - X_1) - X_{plane}(1)}{d_x} \\ j(m) &= 1 + \frac{Y_1 + \alpha_{mid} \cdot (Y_2 - Y_1) - Y_{plane}(1)}{d_y} \end{aligned} \quad (1.38)$$

And with this we are armed with all possible knowledge on the system's geometry. Now let's integrate everything and gather our thoughts:

- Tomographic imaging is the set of techniques with which we can create the image of an object by using said object's projection data;
- Projections are line integrals. They capture how a target body interferes with some kind of known radiation along a given line, which constitutes a ray;
- Projections are always indexed to an emitter and a receiver, which have perfectly determined positions;
- With the positions of the emitters, the **ROI** grid and the Siddon algorithm, we can determine how exactly is each **ROI** pixel traversed by each one of the rays;
- Summing all the lengths of all the pixels traversed by each ray gives us the optical path of said ray;
- Multiplying the length of a ray within a pixel with that pixel's density gives us how that particular pixel interferes with the radiation;
- A projection (remember, a line integral) can be approximated by the sum of all these individual contributions by particular pixels - and this is exactly what is meant by Equation 1.29.

So here we have it. The last piece of the puzzle proposed by Equation 1.25. The discretisation process, namely Siddon's algorithm, allows us to determine the system matrix, \mathbf{a} in this equation.

BIBLIOGRAPHY

- [1] A. Andersen. “Simultaneous Algebraic Reconstruction Technique (SART): A superior implementation of the ART algorithm”. In: *Ultrason. Imaging* 6.1 (Jan. 1984), pp. 81–94. ISSN: 01617346. DOI: 10.1016/0161-7346(84)90008-7. URL: <https://linkinghub.elsevier.com/retrieve/pii/0161734684900087> (cit. on p. 22).
- [2] M. N. Asl and A. Sadremomtaz. “Analytical image reconstruction methods in emission tomography”. In: *J. Biomed. Sci. Eng.* 06.01 (2013), pp. 100–107. ISSN: 1937-6871. DOI: 10.4236/jbise.2013.61013. URL: <http://www.scirp.org/journal/doi.aspx?DOI=10.4236/jbise.2013.61013> (cit. on p. 19).
- [3] Avantes. *Avantes OEM Spectrometers*. 2022. URL: <https://www.avantes.com/products/oem-products/> (cit. on pp. 4, 5).
- [4] C. Beekman. “Differential Optical Absorption Spectroscopy of Trace Gas Species and Aerosols in the Upper Ohio River Valley”. PhD thesis. Ohio State University, 2010 (cit. on pp. 13–15).
- [5] R. T. Brinkmann. “Rotational Raman scattering in planetary atmospheres”. In: *Astrophys J* 154 (1968), pp. 1087–1093. ISSN: 0004-637X. DOI: 10.1086/149827 (cit. on p. 7).
- [6] P. P. Bruyant. “Analytic and iterative reconstruction algorithms in SPECT.” In: *J. Nucl. Med.* 43.10 (2002), pp. 1343–58. URL: <http://www.ncbi.nlm.nih.gov/pubmed/12368373> (cit. on p. 22).
- [7] P. P. Bruyant. “Analytic and iterative reconstruction algorithms in SPECT.” In: *J. Nucl. Med.* 43.10 (2002), pp. 1343–58. ISSN: 0161-5505. URL: <http://jnm.snmjournals.org/cgi/content/abstract/43/10/1343%7B%5C%7D5Cnhttp://jnm.snmjournals.org/cgi/content/full/43/10/1343%7B%5C%7D5Cnhttp://www.ncbi.nlm.nih.gov/pubmed/12368373> (cit. on pp. 17, 22).
- [8] M. Buchwitz et al. “Global carbon monoxide as retrieved from SCIAMACHY by WFM-DOAS”. In: *Atmos. Chem. Phys.* 4.7 (Sept. 2004), pp. 1945–1960. ISSN: 16807316. DOI: 10.5194/acp-4-1945-2004. URL: www.atmos-chem-phys.org/acp/4/1945/ (cit. on pp. 11, 12).

BIBLIOGRAPHY

- [9] M. Buchwitz, V. V. Rozanov, and J. P. Burrows. “A near-infrared optimized DOAS method for the fast global retrieval of atmospheric CH₄, CO, CO₂, H₂O, and N₂O total column amounts from SCIAMACHY Envisat-1 nadir radiances”. In: *J. Geophys. Res. Atmos.* 105.D12 (June 2000), pp. 15231–15245. ISSN: 01480227. DOI: 10.1029/2000JD900191. URL: <http://doi.wiley.com/10.1029/2000JD900191> (cit. on pp. 11, 12).
- [10] K. Chance and R. L. Kurucz. “An improved high-resolution solar reference spectrum for earth’s atmosphere measurements in the ultraviolet, visible, and near infrared”. In: *J. Quant. Spectrosc. Radiat. Transf.* 111.9 (2010), pp. 1289–1295. ISSN: 00224073. DOI: 10.1016/j.jqsrt.2010.01.036. URL: <http://dx.doi.org/10.1016/j.jqsrt.2010.01.036> (cit. on p. 16).
- [11] T. Danckaert et al. *QDOAS*. 2015. URL: <http://uv-vis.aeronomie.be/software/QDOAS/> (cit. on pp. 7, 13).
- [12] M. Defrise, P. E. Kinahan, and C. J. Michel. *Positron Emission Tomography*. Ed. by D. L. Baley et al. London: Springer London, 2005, pp. 63–91 (cit. on pp. 17, 22).
- [13] E. Frins et al. “Tomographic multiaxis-differential optical absorption spectroscopy observations of Sun-illuminated targets: a technique providing well-defined absorption paths in the boundary layer”. In: *Appl. Opt.* 45.24 (Aug. 2006), p. 6227. ISSN: 0003-6935. DOI: 10.1364/AO.45.006227. URL: <https://www.osapublishing.org/abstract.cfm?URI=ao-45-24-6227> (cit. on p. 10).
- [14] J. F. GRAINGER and J. RING. “Anomalous Fraunhofer Line Profiles”. In: *Nature* 193.4817 (Feb. 1962), pp. 762–762. ISSN: 0028-0836. DOI: 10.1038/193762a0. URL: <http://www.nature.com/doifinder/10.1038/193762a0> (cit. on p. 7).
- [15] R. Gunderman. *Essential Radiology: Clinical Presentation, Pathophysiology, Imaging*, 2nd ed. 2nd ed. Thieme, 2006. ISBN: 9781588900821 (cit. on p. 16).
- [16] E. Hecht. *Optics*. 5th. Pearson, 2016. ISBN: 0133977226 (cit. on pp. 3, 4).
- [17] G. T. Herman. “Image Reconstruction From Projections”. In: *Real-Time Imaging* 1.1 (1995), pp. 3–18. ISSN: 10772014. DOI: 10.1006/rtim.1995.1002 (cit. on p. 17).
- [18] G. T. Herman. *Fundamentals of Computerized Tomography. Advances in Pattern Recognition*. London: Springer London, 2009. ISBN: 978-1-85233-617-2. DOI: 10.1007/978-1-84628-723-7. URL: <http://link.springer.com/10.1007/978-1-84628-723-7> (cit. on p. 17).
- [19] G. T. Herman, A. Lent, and S. W. Rowland. “ART: Mathematics and applications. A report on the mathematical foundations and on the applicability to real data of the algebraic reconstruction techniques”. In: *J. Theor. Biol.* 42.1 (1973). ISSN: 10958541. DOI: 10.1016/0022-5193(73)90145-8 (cit. on pp. 17, 20).
- [20] A. C. Kak. “Algebraic Reconstruction Algorithms”. In: *Comput. Tomogr. Imaging*. 2001, pp. 275–296. ISBN: 978-0-89871-494-4. DOI: 10.1137/1.9780898719277.ch7 (cit. on pp. 16, 17, 20–22).

- [21] A. C. Kak and M. Slaney. *Principles of Computerized Tomographic Imaging*. 1. Society for Industrial and Applied Mathematics, Jan. 2001, pp. 49–112. ISBN: 978-0-89871-494-4. DOI: [10.1137/1.9780898719277](https://doi.org/10.1137/1.9780898719277). URL: <http://pubs.siam.org/doi/book/10.1137/1.9780898719277> (cit. on pp. 18, 21).
- [22] A. Merlaud. “Development and use of compact instruments for tropospheric investigations based on optical spectroscopy from mobile platforms”. In: *Books.Google.Com* (2013). URL: <http://books.google.com/books?hl=en%7B%5C&%7Dlr=%7B%5C&%7Did=inXVSyR82zwC%7B%5C&%7Doi=fnd%7B%5C&%7Dpg=PR3%7B%5C&%7Ddq=Development+and+use+of+compact+instruments+for+tropospheric+investigations+based+on+optical+spectroscopy+from+mobile+platforms+sciences%7B%5C&%7Dots=VdebeDBQM%7B%5C&%7Dsig=4G0eVEvthJXuqd8WI3IWjjVXuXc> (cit. on pp. 5–9, 13).
- [23] U. Platt and J. Stutz. *Differential Optical Absorption Spectroscopy*. 2007. ISBN: 9783540211938 (cit. on pp. 5, 6, 8–11).
- [24] W. H. Press et al. *Numerical Recipes: The Art of Scientific Computing*. 3rd Editio. 2007. ISBN: 9788578110796. arXiv: [arXiv:1011.1669v3](https://arxiv.org/abs/1011.1669v3) (cit. on p. 8).
- [25] J. Radon. “On the determination of functions from their integral values along certain manifolds”. In: *IEEE Trans. Med. Imaging* 5.4 (Dec. 1986), pp. 170–176. ISSN: 0278-0062. DOI: [10.1109/TMI.1986.4307775](https://doi.org/10.1109/TMI.1986.4307775). URL: <http://ieeexplore.ieee.org/document/4307775/> (cit. on p. 16).
- [26] V. Rozanov et al. “Sciatran - a new radiative transfer model for geophysical applications in the 240–2400 NM spectral region: the pseudo-spherical version”. In: *Adv. Sp. Res.* 29.11 (June 2002), pp. 1831–1835. ISSN: 02731177. DOI: [10.1016/S0273-1177\(02\)00095-9](https://doi.org/10.1016/S0273-1177(02)00095-9). URL: <https://linkinghub.elsevier.com/retrieve/pii/S0273117702000959> (cit. on p. 11).
- [27] L. A. Shepp and Y. Vardi. “Maximum Likelihood Reconstruction for Emission Tomography”. In: *IEEE Trans. Med. Imaging* 1.2 (Oct. 1982), pp. 113–122. ISSN: 0278-0062. DOI: [10.1109/TMI.1982.4307558](https://doi.org/10.1109/TMI.1982.4307558). URL: <https://ieeexplore.ieee.org/document/4307558/> (cit. on p. 22).
- [28] R. L. Siddon. “Fast calculation of the exact radiological path for a three-dimensional CT array”. In: *Med. Phys.* 12.2 (Mar. 1985), pp. 252–255. ISSN: 00942405. DOI: [10.1118/1.595715](https://doi.org/10.1118/1.595715). URL: [http://doi.wiley.com/10.1118/1.595715](https://doi.wiley.com/10.1118/1.595715) (cit. on p. 23).
- [29] W. J. Smith. *Modern Optical Engineering - The Design of Optical Systems*. 3rd. Carisbad, California: McGraw-Hill, 2000. ISBN: 0071363602 (cit. on p. 4).
- [30] R. Valente de Almeida, N. Matela, and P. Vieira. “TomoSim: A Tomographic Simulator for Differential Optical Absorption Spectroscopy”. In: *Drones* 5.1 (Dec. 2020), p. 3. ISSN: 2504-446X. DOI: [10.3390/drones5010003](https://doi.org/10.3390/drones5010003). URL: <https://www.mdpi.com/2504-446X/5/1/3> (cit. on p. 21).
- [31] R. Valente de Almeida and P. Vieira. “Forest Fire Finder – DOAS application to long-range forest fire detection”. In: *Atmos. Meas. Tech.* 10.6 (June 2017), pp. 2299–2311. ISSN: 1867-8548. DOI: [10.5194/amt-10-2299-2017](https://doi.org/10.5194/amt-10-2299-2017). URL: <https://www.atmos-meas-tech.net/10/2299/2017/> (cit. on pp. 5, 8).

BIBLIOGRAPHY

